J. Fluid Mech. (2004), *vol.* 507, *pp.* 175–202.
DOI: 10.1017/S0022112004008833 Printed in the United Kingdom

Experimental and numerical study of the shear layer instability between two counter-rotating disks

By F. MOISY[1], O. DOARÉ[1]†, T. PASUTTO[1], O. DAUBE[2] AND M. RABAUD[1]

[1]Laboratoire FAST, Bâtiment 502, Campus Universitaire, F-91405 Orsay Cedex, France

[2]CEMIF/LME, Université d'Evry, 40 Rue du Pelvoux, F-91020 Evry Cedex, France

(Received 8 September 2003 and in revised form 5 January 2004)

The shear layer instability in the flow between two counter-rotating disks enclosed by a cylinder is investigated experimentally and numerically, for radius-to-height ratio $\Gamma = R/h$ between 2 and 21. For sufficiently large rotation ratio, the internal shear layer that separates two regions of opposite azimuthal velocities is prone to an azimuthal symmetry breaking, which is investigated experimentally by means of visualization and particle image velocimetry. The associated pattern is a combination of a sharp-cornered polygonal pattern, as observed by Lopez *et al.* (2002) for low aspect ratio, surrounded by a set of spiral arms, first described by Gauthier *et al.* (2002) for high aspect ratio. The spiral arms result from the interaction of the shear layer instability with the Ekman boundary layer over the faster rotating disk. Stability curves and critical modes are experimentally measured for the whole range of aspect ratios, and are found to compare well with numerical simulations of the three-dimensional time-dependent Navier–Stokes equations over an extensive range of parameters. Measurements of a local Reynolds number based on the shear layer thickness confirm that a shear layer instability, with only weak curvature effect, is responsible for the observed patterns. This scenario is supported by the observed onset modes, which scale as the shear layer radius, and by the measured phase velocities.

1. Introduction

The stability of the flows between rotating disks, or von Kármán (1921) swirling flows, has been addressed for a long time, mostly in the rotor–stator configuration, i.e. between one rotating and one stationary disks (Zandbergen & Dijkstra 1987). Of practical interest for laboratory experiments is the case of finite disks, for which no similarity solutions exist. The nature and the stability of the flow then strongly depends on the radius-to-height ratio, $\Gamma = R/h$, and the rotation ratio, $s = \Omega_b/\Omega_t$ (t and b refer to the top and bottom disks respectively). Most of the studies deal with the rotor–stator configuration, $s = 0$, and it is only recently that the intermediate cases, $-1 < s < 1$, have been addressed experimentally and numerically (Lopez 1998; Lopez *et al.* 2002; Gauthier *et al.* 2002; Nore *et al.* 2003, 2004). Other parameters may also be taken into account, such as the presence of a central hub or the end condition of the sidewall; these extra parameters are of practical importance, for instance in hard

† Present address: ENSTA/UME, Chemin de la Hunière, F-91761 Palaiseau Cedex, France.

disk systems, for which $\Gamma \sim O(10)$ and $s = 1$ (Humphrey, Schuler & Webster 1995), or turbomachines. The quasi-solid-body rotation limit, $s \approx 1$, is of great importance in geophysical flows (Stewartson 1953; Hide & Titman 1967; Früh & Read 1999).

The investigation of the flow in rotor–stator $\Gamma \sim O(1)$ cavities has been mainly motivated by the experimental observation of vortex breakdown in the form of recirculatory bubble by Escudier (1984). The axisymmetry breaking of the base flow gives rise to rotating waves, analysed in detail by Gelfgat, Bar-Yoseph & Solan (2001), Blackburn & Lopez (2002) and Serre & Bontoux (2002) for $\Gamma < 1$. For flatter cavities, $\Gamma \sim O(10)$, the recent experimental studies have mainly focused on the boundary layer instabilities in the rotor–stator case (Gauthier, Gondret & Rabaud 1999; Schouveiler, Le Gal & Chauve 2001), further characterized numerically by Serre, Crespo del Arco & Bontoux (2001). Two classes of instability are observed: axisymmetric propagating vortices and positive spirals. These studies have been extended to differential rotation of the disks by Gauthier *et al.* (2002) for $\Gamma = 20.9$. It was shown that co-rotating and weak counter-rotating flows only weakly affect the properties of the boundary layer instabilities, like linearly shifting the instability thresholds or the onset modes.

The flow between counter-rotating disks appears to be much richer: in addition to the boundary layer instabilities, free shear layer instabilities also take place, which have been the subject of much recent experimental and numerical effort. In the simplest flow configuration, with exact counter-rotating disks and a stationary sidewall, the axisymmetric base flow becomes unstable through a Kelvin–Helmholtz instability of the equatorial free shear layer, giving rise to radial co-rotating vortices. The complete scenario of bifurcations in this configuration, for aspect ratios Γ between $1/2$ and 3, has been numerically investigated by Nore *et al.* (2003, 2004).

In the less symmetric case of counter-rotating disks with a rotating sidewall and arbitrary rotation ratio, the instability mechanism basically remains the same, although the geometry of the internal shear layer becomes more complex. The main difference is that a sufficiently large rotation ratio is needed for the transition layer to detach from the slower rotating disk and give rise to a free shear layer. The reason is that for sufficiently large rotation ratio, the structure of the meridional flow drastically changes, evolving from a one-cell to a two-cell recirculation flow, with a stagnation circle on the slower disk, which is responsible for the detachment of the shear layer into the bulk of the flow. This property was first described experimentally and numerically by Dijkstra & van Heijst (1983) for $\Gamma = 14.3$, and further characterized by Lopez (1998) for $2 \leqslant \Gamma \leqslant 8$ from axisymmetric numerical simulations.

Detailed investigation of the instability of this internal shear layer by means of dye visualization and three-dimensional numerical simulations, restricted to $\Gamma = 2$ and $\Omega_t h^2/\nu = 250$, has been performed by Lopez *et al.* (2002) and Marques, Gelfgat & Lopez (2003). These authors observed patterns of wavenumber 4 and 5, in the form of funnel-like vortices. At the same time, for a very different aspect ratio $\Gamma = 20.9$, Gauthier *et al.* (2002) reported a new instability pattern of wavenumber 9 to 11, in the form of a set of spiral arms. This pattern was given the name of 'negative' spirals, because they roll up to the centre in the direction of the slower disk. Although the morphology of the funnel-like vortices and the negative spirals patterns strongly differs, the issue of a possible continuity between them was first raised by Gauthier *et al.* (2002) and Moisy, Pasutto & Rabaud (2003). The purpose of this paper is to address this issue from a detailed analysis of the instability patterns for a wide range of aspect ratio Γ, between 2 and 21.

The influence of the curvature and rotation on the stability of internal shear layers has received considerable interest (Dolzhanskii, Krymov & Manin 1990). In addition

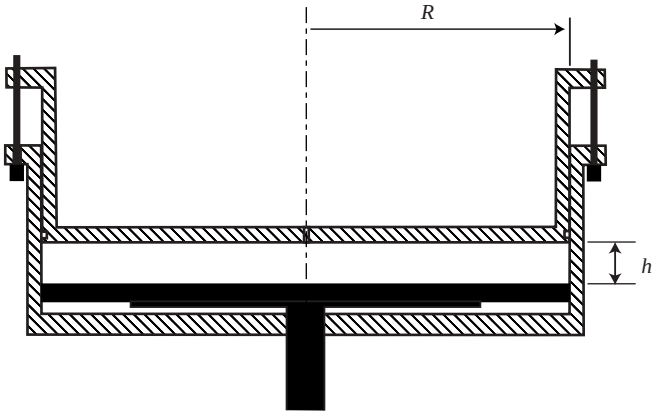

FIGURE 1. Experimental cell. The cylinder (hatched regions), made of transparent Plexiglas, rotates with angular velocity Ω_t, while the bottom disk (black) rotates in the opposite sense with angular velocity Ω_b.

to the classical Kelvin–Helmholtz instability, centrifugal effects may also occur, which are stabilizing or destabilizing (Yanase *et al.* 1993; Liou 1994). The extreme case where rotation dominates the dynamics plays a central role in geophysical flows. After the pioneering study of Hide & Titman (1967), laboratory experiments focused on weak shear compared to the background rotation, showing patterns in the form of circular chains of eddies, with complex nonlinear mode selection and eddy clustering (Niino & Misawa 1984; Konijnenberg *et al.* 1999; Früh & Read 1999). Closer to our experiment, Rabaud & Couder (1983) have investigated the stability of a two-dimensional forced circular shear layer in a split-annulus tank without background rotation, further studied numerically by Chomaz *et al.* (1988) and Bergeron *et al.* (2000). Although in these experiments the rotation only weakly affects the shear layer instability, patterns in the form of circular chains of eddies are observed as well, the number of which decreases as the Reynolds number is increased.

The outline of the paper is as follows: § 2 briefly presents the experimental set-up, and § 3 summarizes the numerical methods. The steady axisymmetric base flow is described in § 4, with special attention paid to the existence domain of the two-cell recirculating flow. Instability patterns and onset curves are described in § 5 from particle image velocimetry (PIV) measurements and numerical simulations. In § 6 the instability is characterized in terms of a local Reynolds number based on the internal shear layer. Systematic measurements of the onset modes and phase velocities are presented, and are shown to compare well with a classical Kelvin–Helmholtz instability mechanism. Some concluding remarks are finally offered in § 7.

2. Experimental set-up

2.1. *Experimental cell*

The experimental cell, sketched in figure 1, is adapted from that of Gauthier *et al.* (2002) to allow lateral visualization and lighting. It consists of a rotating cylinder of radius $R = 140$ mm, in which a disk of the same radius located at the bottom of the cavity rotates at a different speed. The cylinder and its upper cover (top disk) are made of Plexiglas, to allow visualizations from above and from the side, while the bottom disk is made of black painted brass to improve the visualization contrast. The thickness

of the cell h can be varied from a few millimetres to 7 cm, using wedges between the upper disk and the cylinder rim.

The angular velocities of the top and bottom disks, Ω_t and Ω_b, can be set independently, from 0 to 10 rad s^{-1}. Since we are only concerned with the counter-rotation flow in the present paper, there is no ambiguity in the sign of the angular velocities, which are taken positive. The upper disk is the faster one, $\Omega_t \geqslant \Omega_b$, throughout the paper, except in § 5.2 where the influence of the rotating sidewall is investigated. For both experimental and numerical visualizations, the flow is seen from above, the upper disk rotates anticlockwise while the bottom one rotates clockwise.

Water–glycerol mixture and silicone oils have been used as working fluids, allowing the spanning of a range of kinematic viscosity ν between 1.0×10^{-6} and 50×10^{-6} m^2 s^{-1} at 20 °C. Viscosity changes due to temperature drift during experiments (about 2% per degree for both glycerol and silicone oils) were controlled, and all the uncertainties finally lead to an accuracy of 3% in the determination of the Reynolds numbers.

2.2. *Dimensionless numbers*

The flow is characterized by three dimensionless numbers: two Reynolds numbers based on each disk velocity and the aspect ratio $\Gamma = R/h$. Since two lengthscales, R and h, are present in this geometry, freedom exists in the definition of the Reynolds numbers. The basic Reynolds numbers are here based on the cell thickness h,

$$Re_i = \Omega_i h^2/\nu, \tag{2.1}$$

where $i = b, t$ denotes the bottom and top disks. In the limit of very large Γ, the cell radius R has a vanishingly small influence on the flow and these Reynolds numbers Re_i are expected to be the relevant control parameters. In particular they allow one to distinguish between separated and merged boundary layers situations. On the other hand, for a flatter cavity $\Gamma \approx O(1)$, both R and h are relevant, so that the Reynolds numbers based on the thickness and the peripheral velocities, $\Gamma Re_i = \Omega_i Rh/\nu$, are also of interest. In the present study, the Reynolds numbers Re_i are of order 10–2000, and the aspect ratio Γ has been varied between 2 and 20.9.

In some cases, the set of parameters (Γ, Re_t, s), where $s = \Omega_b/\Omega_t = Re_b/Re_t$ is the counter-rotation ratio, is more convenient than (Γ, Re_t, Re_b). Since we are only concerned with the counter-rotation case here, the ratio s is taken always positive. Note that this definition contrasts with the one adopted by Gauthier *et al.* (2002), where $s < 0$ was taken for the counter-rotating regime and $s > 0$ for the co-rotating regime.

2.3. *Measurement techniques*

Qualitative insight into the flow structure is obtained from visualization of the light reflected by anisotropic flakes seeding the flow. We make use of Kalliroscope† when the working fluid is water–glycerol mixture, and Iriodin‡ when it is silicone oil. The flow is illuminated by a concentric circular light source, and pictures are obtained using a CCD camera located above, along the disk axis.

More quantitative measurements have been performed using a particle image velocimetry (PIV) apparatus¶. Small borosilicate particles, 11 μm in diameter, seeding the flow are used as tracer, illuminated by a laser sheet of thickness 0.5 mm produced

† Kalliroscope Corporation, 264 Main Street, Box 60, Groton, MA 01450, USA.
‡ Iriodin: Pigments sold by Merck Corporation.
¶ Flowmaster 3, LaVision GmbH, Anna-Vandenhoeck-Ring 19, D-37081 Goettingen, Germany.

by a double-pulsed Nd:Yag (25 mJ/pulse) and a cylindrical lens. Images are acquired with a double-buffer high-resolution camera (12 bits, 1280×1024 pixels), synchronized with the laser at a rate of 4 frame pairs per second. The velocity fields are averaged over four successive individual fields, i.e. for 1 s, a value much lower than the characteristic timescale of the flow.

The structure of the axisymmetric base flow in the meridional plane is obtained with a vertical laser sheet lighting. The cylindrical wall allows undistorted pictures in the central part of the cell, $r \leqslant 0.7R$. The important out-of-plane azimuthal velocity component strongly constrains the time delay between two succesive frames, of order 4 ms. A resolution of 0.5 mm can be achieved, except near the disks where the important vertical gradient and out-of-plane velocity component prevent resolution of the boundary layers. The bifurcated patterns are investigated using horizontal laser sheet lighting between the two disks and the camera above. For these measurements, a sufficiently large disk separation h and a perfectly horizontal laser sheet are required due to the important vertical gradients. For these reasons, systematic measurements were only possible for low aspect ratio, $\Gamma = 3$ and 7. Another important constraint arises from the important variability in the velocity, from mm s^{-1} near the centre up to 10 cm s^{-1} in periphery, making difficult the choice of a unique time delay between the frames and window size for the PIV computations. Typical time delays of order of 30 ms were chosen for measurements near the centre, where the instability patterns essentially occur.

3. Numerical method

The numerical simulations of the three-dimensional flow between counter-rotating disks for various aspect ratios have been carried out by solving the time-dependent Navier–Stokes equations. In addition, a linear stability analysis of the steady axisymmetric base flow has also been performed. These calculations were performed along the lines of the general methodology developed in Gadoin, Le Quéré & Daube (2001), Daube & Le Quéré (2002) and Nore *et al.* (2003), to numerically investigate flow instabilities. For this purpose, several computational tools have been used, which are based upon the use of the same spatial discretization; details may be found in Barbosa & Daube (2001).

3.1. *Spatial discretization*

The different unknowns are first expanded in truncated Fourier series over N modes in the azimuthal direction. The coefficients of this expansion are then discretized in the (r, z)-planes by means of mimetic finite difference operators (Hyman & Shashkov 1997):

(i) A staggered, uniform or non-uniform, grid in cylindrical coordinates (r, θ, z) is used. The only unknown located on the axis $r = 0$ is the axial component ω_z of the vorticity, therefore avoiding the singularity at $r = 0$, since no terms containing $1/r$ have to be considered on the axis.

(ii) The first-order divergence and curl differential operators are discretized by means of the Gauss and Stokes theorems written on elementary cells and the second-order differential operators are constructed as compounds of these first-order discrete operators.

(iii) The nonlinear terms are written as $(\nabla \times \boldsymbol{v}) \times \boldsymbol{v}$ and discretized such that they do not contribute to energy production, as in the continuum case. They are classically computed in the physical space with the usual 3/2 rule.

3.2. *Computation of the base flow*

Since the computation of the steady axisymmetric base flow is needed, even when it is unstable, the usual procedure, which consists of obtaining steady-state solutions by letting $t \to \infty$ in a time-stepping code, must be rejected in favour of a Newton–Raphston method. The main drawback of this approach is that the Jacobian matrix of the Navier–Stokes operator is huge and ill-conditioned. To overcome these difficulties, we have used the Stokes preconditioned Newton method proposed by Tuckerman (1989) and Mamum & Tuckerman (1995).

3.3. *Time discretization*

Since we are primarily interested in the transition to unsteadiness, the temporal scheme is of great importance. We use a second-order time-marching procedure with an implicit discretization of the linear terms and an explicit Adams–Bashforth-type extrapolation of the nonlinear terms. This procedure is used for both the full nonlinear and the linearized computations. The computation of each time step therefore amounts to the resolution of a so-called generalized Stokes problem for $(\boldsymbol{v}^{n+1}, p^{n+1})$, the values of the velocity and of the pressure at time $(n+1)\Delta t$:

$$\left.\begin{aligned} &\left(\frac{3Re}{2\Delta t}\boldsymbol{I} - \nabla^2\right)\boldsymbol{v}^{n+1} + \nabla p^{n+1} = \boldsymbol{S}^{n,n-1}, \\ &\nabla \cdot \boldsymbol{v}^{n+1} = 0. \end{aligned}\right\} \tag{3.1}$$

The source terms $\boldsymbol{S}^{n,n-1}$ contain all the quantities which were evaluated at the previous time steps. In this time-discretized problem, the velocity–pressure coupling is handled by means of an incremental projection method (Goda 1979; Daube & Le Quéré 2002).

3.4. *Computational features*

Both uniform and non-uniform grids are used, depending on the aspect ratio $\Gamma = R/h$. For moderate aspect ratio, $\Gamma \leqslant 10$, a uniform grid is found to be sufficient. For instance, the computations for $\Gamma = 7$ have been carried out on a uniform grid (r, θ, z), with a resolution of $401 \times 32 \times 101$.

For larger aspect ratio, a non-uniform grid is used. The meshes in the z-direction are defined by means of a double hyperbolic tangent function, allowing refinement both in the boundary layers along the disks and in the sheared region at mid-height of the cavity. In the r-direction, the grid is uniform up to $r = 3R/4$ and then geometrically refined up to the sidewall. A maximum resolution of $513 \times 78 \times 97$ has been used in the case $\Gamma = 21$.

The time steps are chosen with respect to stability considerations, yielding a number of time steps per revolution within the range 500–1000. Noteworthy is the fact that using a second-order time stepping ensures the independence of the results with respect to the time step.

4. Base flow

4.1. *Structure of the meridional flow*

We first focus on the steady axisymmetric base flow in the counter-rotating regime, by means of PIV measurements and numerical simulation of the axisymmetric Navier–Stokes equations.

Superimposed on the essentially azimuthal velocity field, each disk tends to impose a meridional recirculation flow. The outward flow induced by the faster disk (here

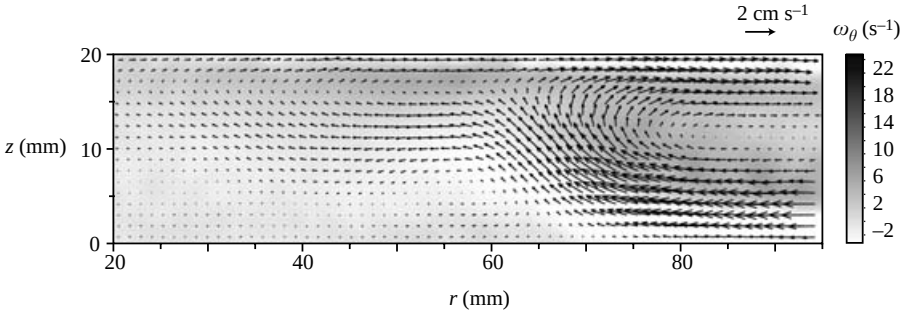

FIGURE 2. Experimental velocity field of the base flow in the meridional plane, and azimuthal vorticity field ω_θ (grey scale), for $\Gamma = 7$, $Re_t = 130$ and $s = 0.154$. Note that only the region $0.14 \leqslant r/R \leqslant 0.68$ is shown.

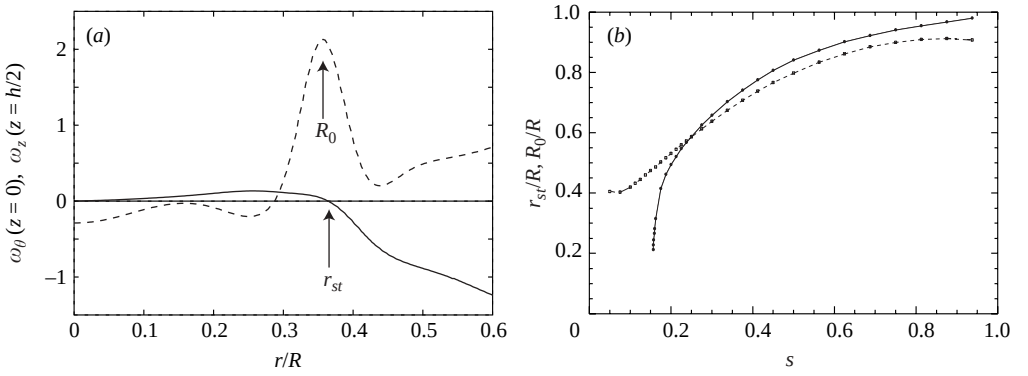

FIGURE 3. (*a*) Vorticity profiles from axisymmetric simulations, illustrating the definitions of the stagnation radius, r_{st}, and the shear layer radius, R_0. —, Azimuthal vorticity ω_θ on the bottom disk $z = 0$; – –, vertical vorticity ω_z at mid-height $z = h/2$. $\Gamma = 7$, $Re_t = 250$, $s = 0.164$ ($Re_b = 41$). (*b*) —, Stagnation radius r_{st}/R; – –, location R_0/R of the maxium of the vertical vorticity at mid-height, as functions of the rotation ratio s, for $\Gamma = 7$, $Re_t = 114$.

the top disk) recirculates at large radius towards the centre of the slower disk due to the lateral confinement. At low rotation ratio, the centrifugal effect of the slower disk is not strong enough to counteract the inward flow from the faster disk, and the meridional flow simply consists of a single recirculating cell, similar to that of the rotor–stator or co-rotating cases. On the other hand, when the rotation ratio is increased above a certain value, the slower disk induces a centrifugal flow too, and the meridional flow becomes organized into a two-cell recirculating structure, associated with a stagnation circle on the slower disk where the radial component of the velocity vanishes, as illustrated by the PIV measurements in figure 2.

In the two-cell regime, the presence of a stagnation circle has important consequences on the structure of the base flow, as can be seen in figure 10(*a*) – that will be described in § 5.3. The axial vorticity at mid-height, $\omega_z(z = h/2)$, plotted in figure 3(*a*) as a function of the radius, shows a pronounced maximum that separates an inner region of low angular velocity, which rotates with the bottom disk, from an outer region which rotates with the faster disk. In the same figure, the azimuthal vorticity profile on the bottom disk, ω_θ ($z = 0$), is also shown. The location where ω_θ crosses zero defines the stagnation radius, r_{st}, separating an inner region, where the

flow close to the bottom disk is outward, from an outer region where it is inward. It appears that the radius of maximum vorticity, R_0, approximately coincides with the stagnation radius. Measurements of R_0 as a function of s, shown in figure 3(b) in the case $\Gamma = 7$, confirm that this radius closely follows the stagnation radius r_{st}. As the rotation ratio is increased, the annular shear layer and the stagnation circle are pushed outward, as the result of the increasing centrifugal effect of the slower disk, and take value close to 1 in the limit of the exact counter-rotation $s \to 1$. However, this figure clearly shows that the shear layer exists for all $s > 0$, while the stagnation circle only exists for sufficiently high rotation ratio, $s \geqslant s_0$. This means that, although the slower disk rotation may not be strong enough to develop an outward recirculation flow, it causes the inward boundary layer to decelerate, leading to a local increase of the vertical velocity. As a consequence, negative angular momentum of the slower (bottom) disk is advected upwards, leading to an annular shear layer even in the absence of a stagnation circle. But in any case, this mechanism is strongly enhanced by the presence of the stagnation circle for $s \geqslant s_0$, which detaches the inward boundary layer into the bulk of the flow, and an intense annular shear layer is encountered when the stagnation circle is present. This annular shear layer is prone to a shear instability that breaks the axisymmetry of the base flow as the rotation ratio s is increased, leading to the flow patterns described in section § 5.

4.2. *Existence domain of the stagnation circle*

The two-cell structure of the counter-rotating flow was first reported by Dijkstra & van Heijst (1983), from axisymmetric simulation and experimental investigation at $\Gamma = 14.3$. Despite a moderate resolution, these authors gave clear evidence of a minimum rotation ratio for the stagnation circle to appear. This was further observed numerically by Lopez (1998) for smaller aspect ratios, $\Gamma = 2$, 4, and 8. Measurements at $\Gamma = 20.9$ were carried out by Gauthier *et al.* (2002) for various Reynolds numbers, and it was suspected that the stagnation circle was always present at the onset of negative spirals. However, due to uncertainty in the experimental method, no clear conclusion on the role of the stagnation circle was drawn. In order to remove this uncertainty, a systematic study of the stagnation circle has been carried out using axisymmetric stationary simulations for Γ ranging from 1 to 28, focusing on its existence domain as function of the parameters (Γ, Re_t, s).

Values of the normalized stagnation radius, r_{st}/R, are shown in figure 4 as a function of the rotation ratio $s = \Omega_b/\Omega_t$ for various values of Re_t (the aspect ratio is kept at $\Gamma = 7$). In the limit of high Reynolds numbers, the different curves collapse into a single master curve, starting from $r_{st} \approx 0$ for $s = s_0 \approx 0.10$. For lower Reynolds numbers, higher values of s, around 0.2–0.5, are needed for the two-cell structure to develop, and the stagnation circle directly appears at a non-zero radius.

The minimum counter-rotation ratio s_0 for various aspect ratios is plotted as a function of Re_t in figure 5. These curves separate the lower part, $s < s_0$, where only one recirculating cell exists, from the upper part, $s \geqslant s_0$, where the two cells are present. On the same figure, experimental determinations of s_0, obtained for $\Gamma = 20.9$ from the data of Gauthier *et al.* 2002 (see their figure 7), are also shown, and compare rather well with the present numerical results.

For sufficiently large aspect ratio, the critical ratio s_0 decreases from $s_0 \approx 0.67 \pm 0.02$ in the limit of low Reynolds numbers, and saturates towards a constant value $s_0 \approx 0.100 \pm 0.003$ for higher Reynolds numbers. It is worth pointing that the $Re_t \to 0$ limit is in excellent agreement with the computation of Dijkstra & van Heijst (1983) (see their Appendix A.3), who predicted a limiting value $s_0 = 2/3$ for the Stokes

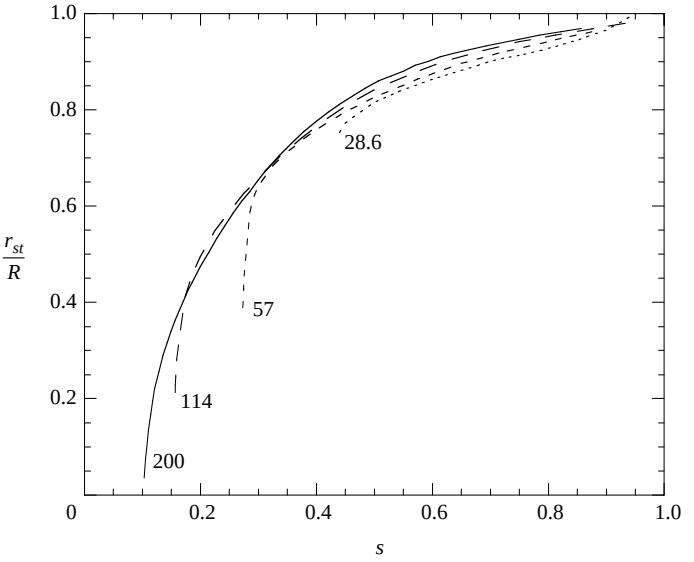

FIGURE 4. Normalized stagnation radius r_{st}/R as a function of the counter-rotation ratio $s = Re_b/Re_t$ for $\Gamma = 7$, from axisymmetric simulations. The corresponding Reynolds number of the top disk, Re_t, is indicated.

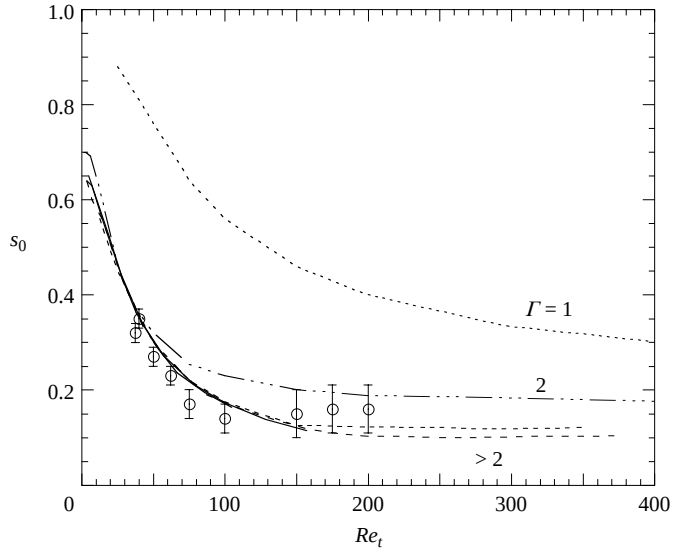

FIGURE 5. Critical counter-rotation ratio s_0 as a function of Re_t. Lines: numerical results, for various aspect ratios, $\Gamma = 1, 2, 4, 7, 14, 21$ and 28 (from top to bottom). ○, Experimental measurements, for $\Gamma = 20.9$.

flow. However, the much larger Reynolds number of their experiments and numerical simulations did not allow them to confirm this result.

The collapse of the different curves $s_0 = f(Re_t)$ for high aspect ratio, $\Gamma > 4$, is remarkable. The reason is that for a flat cavity, the radius R does not play an important role in the flow structure, so that the Reynolds number $Re_t = \Omega_t h^2/\nu$ based on the thickness h is the only relevant parameter in the problem. This similarity breaks

for lower aspect ratio, around $\Gamma < 4$, for which the minimum counter-rotation ratio s_0 significantly increases, suggesting a stabilizing influence of the sidewall on the stagnation circle formation.

In the high aspect ratio case, the crossover between the Stokes regime, where $s_0 \to 2/3$, and the higher Reynolds number regime, where $s_0 \approx 0.10$, takes place at $Re_t \approx 60$. Above this crossover, separated boundary layers appear over each disk, with $\delta_t + \delta_b < h$, where δ_t and δ_b are the top and bottom boundary layer thickness. Both δ_t and δ_b are controlled by the faster disk, and scale as $\delta = (\nu/\Omega_t)^{1/2}$. Using the values $\delta_t/\delta \simeq 2.2$ and $\delta_b/\delta \sim 4.5$ reported by Gauthier *et al.* (2002) gives a rough estimate for the transition Reynolds number,

$$Re_t = \Omega_t h^2/\nu \approx (2.2 + 4.5)^2 \approx 45. \tag{4.1}$$

Although slightly smaller, this value is of the same order as the crossover $Re_t \approx 60$ in figure 5. One may conclude that, for $Re_t > 60$, the stagnation radius results from the competition between well-defined boundary layers, while for $Re_t < 60$ it results from purely viscous effects.

5. Instability patterns

5.1. *Visualizations*

On increasing the Reynolds number, the axisymmetric base flow becomes unstable, leading to instability patterns that can be visualized from the light reflected from the anisotropic flakes, as shown in figure 6 for aspect ratio $\Gamma = R/h$ ranging from 6.1 to 20.9.

The instability patterns basically consist of a sharp-cornered polygon of m sides, surrounded by a set of $2m$ outer spiral arms. However, the combination of these two aspects of the pattern can only be seen simultaneously for some modes and values of the aspect ratio. The lower modes observed for low aspect ratio essentially show the polygon pattern (figure 6*a–c*, with $m = 3$, 4 and 5), similar to those observed by Lopez *et al.* (2002) at $\Gamma = 2$ using dye visualization. In figure 6(*b*), both the $m = 4$-sided polygon and the surrounding $2m = 8$ spiral arms can be seen. In addition a set of m inner arms connecting the corners of the polygon to the centre also appears, which become spiral arms as the aspect ratio Γ is increased (figure 6*d–f*, with $m = 7$ and 11). Both the m inner arms and the $2m$ outer arms can be seen in figure 6(*f*), and the corners of the polygon appear as bright V-shaped patterns where the m arms split into $2m$ arms. On the other hand only the m inner spiral arms can be seen in figure 6(*e*). In this figure the polygon and the outer spiral arms extend to larger radii, where visualization is not possible due to the cylindrical rim.

The spiral arms seen here correspond to the negative spirals described by Gauthier *et al.* (2002), where the observations were restricted to $\Gamma = 20.9$. The name of 'negative' spirals has been chosen because they roll up to the centre in the direction of the slower disk – but also to distinguish them from the positive spirals, a pattern that arises from an instability of the inward boundary layer close to the slower disk, and which is also present in the rotor–stator and co-rotating flows.

Close to the onset, the pattern slowly rotates as a whole, in the sense of the faster or the slower disk, with an angular velocity of order of one tenth of the faster rotating disk. Measurements of phase velocities are given in § 6.3. As the Reynolds number is increased slightly beyond their transition values, higher-order modes quickly superimpose on the fundamental one, eventually leading to a disordered pattern. Only

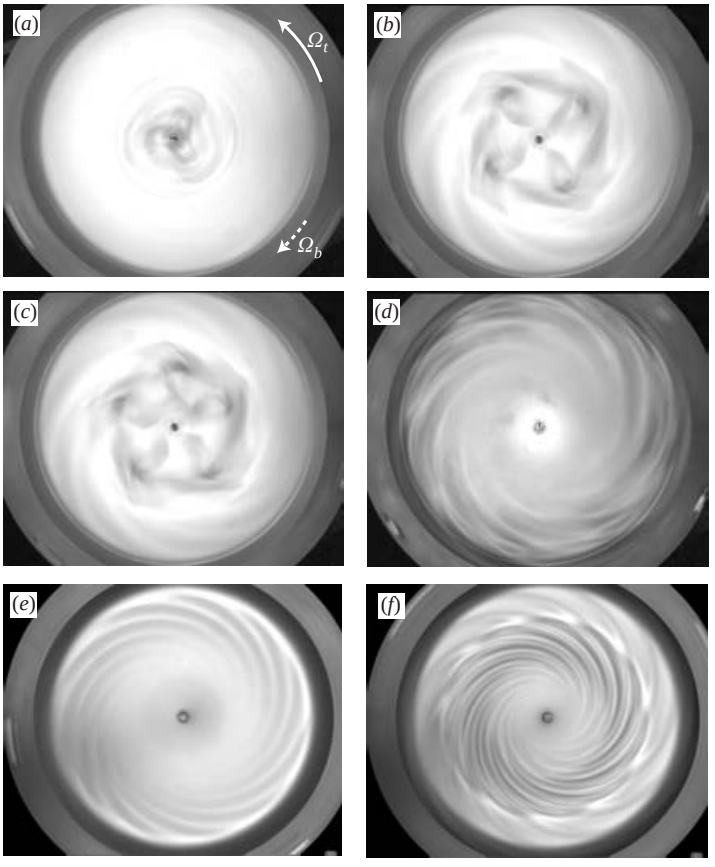

FIGURE 6. Instability patterns visualized by seeding flakes. (*a*) $(\Gamma, Re_t, Re_b) = (6.1, 584, 79)$, showing a mode $m = 3$. (*b*) (7, 282, 47.1), $m = 4$. (*c*) (7, 282, 51.8), $m = 5$. (*d*) (10.8, 60.6, 26.8), $m = 7$. (*e*) (20.9, 46, 10.5), $m = 11$. (*f*) (20.9, 74, 13.6), $m = 11$. The flow is only visible on a central region, $r \leqslant 0.83R$, due to the shadow from the cylindrical rim. Disk rotations are indicated by the arrows in (*a*).

the patterns at the onset are considered here, and the Reynolds numbers are kept close to that for the onset of the instability.

The relationship between the light intensity reflected by the flakes and the velocity gradient tensor field of the flow is non-trivial in the general case (Gauthier, Gondret & Rabaud 1998). Although the intensity field may represent the depth-averaged orientation of the flakes, screening effects from the upper regions may considerably alter the interpretation of the observed patterns, so that the three-dimensional flow structure cannot be directly inferred from the visualizations of figure 6. This visualization method is nevertheless convenient as a first approach, as it allows us to easily define the domains of parameters of interest where more quantitative measurements are to be performed.

5.2. *Onset curves*

The experimental onset curves of the patterns are shown in figure 7 in the plane of parameters (Re_t, Re_b) for various aspect ratios Γ ranging between 2 and 20.9. These curves are obtained by slowly increasing the bottom disk angular velocity Ω_b at fixed value of Ω_t and visually inspecting the intensity pattern of the light reflected by the

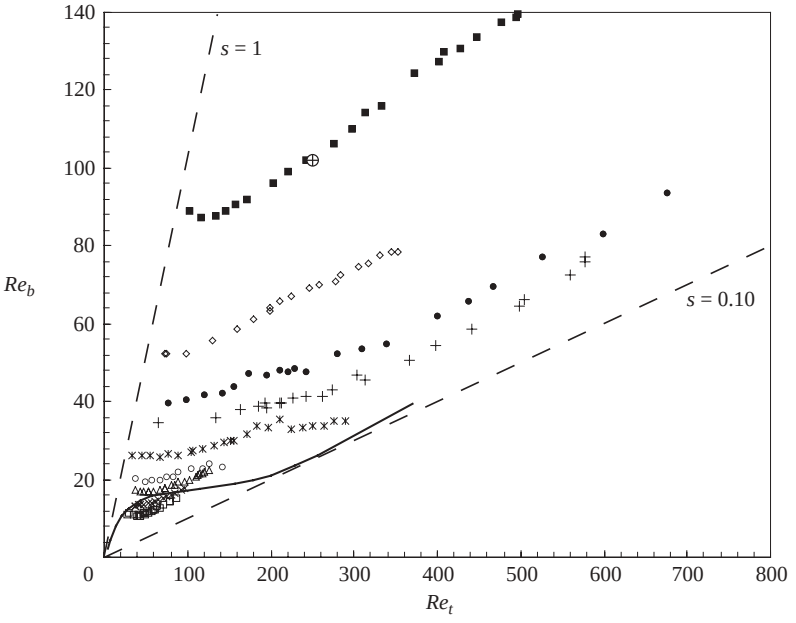

FIGURE 7. Stability curves for various aspect ratios $\Gamma = R/h$ from 2 to 21. ■, $\Gamma = 2$; ◇, 3; ●, 5.2; +, 7; ⋆, 9.3; ○, 12.6; △, 14.4; ×, 18; □, 20.9; ⊕, Instability threshold obtained by Lopez *et al.* (2002), at $\Gamma = 2$. The continuous line indicates the stagnation circle onset for $\Gamma = 7$, and separates the one-cell domain (lower region) from the two-cell domain (upper region). The dashed lines indicate the exact counter-rotation slope, $s = 1$, and the slope $s = s_0 \simeq 0.10$ corresponding to the onset of the two-cell structure at high Reynolds number.

flakes. No hysteresis is observed within our experimental uncertainty, of around 3%. The scatter mainly originates from the very large growth time of the instability close to the onset, which can be as large as 100 rotation periods of the faster disk. For high aspect ratio, boundary layer instabilities arise at moderate Reynolds numbers, and the onset curves for the shear layer instability become defined only for a restricted range of Re_t. It is worth pointing out that, although no hysteresis is observed for the instability threshold, noticeable hysteresis is present for the onset mode, which will be described in § 6.2. The point $(\Gamma, Re_t, Re_b) = (2, 250, 102)$ obtained by Lopez *et al.* (2002), also shown in figure 7, is in excellent agreement with the present results.

In the same figure the line separating the one-cell and two-cell domains is also plotted for $\Gamma = 7$. This curve is given by $Re_b = s_0 Re_t$, where $s_0(\Gamma, Re_t)$ is the minimum rotation ratio for the two-cell structure and the associated stagnation circle to appear (see figure 5). Similar curves are obtained for other aspect ratios, not shown here for clarity. From figure 7 it appears that the stability curves essentially fall into the two-cell domain, except for the highest aspect ratio, around $\Gamma > 16$, for which the instability arises in the upper part of the one-cell domain. Note that, for low aspect ratios, the presence of the two-cell structure is not a sufficient condition for the base flow to become unstable, and a much higher Re_b is needed for the instability to arise.

Figure 8 shows the same data as in figure 7, but plotted in the plane of parameters $(\Gamma Re_t, \Gamma Re_b)$. Using this new set of parameters, the onset curves tend to collapse reasonably well, except for those corresponding to the lowest aspect ratios, $\Gamma = 2$ and 3, which significantly depart from it. The curves start from $\Gamma Re_b \approx 200 \pm 40$ and collapse towards a constant rotation ratio line, $s \approx 0.13 \pm 0.01$, slightly beyond the

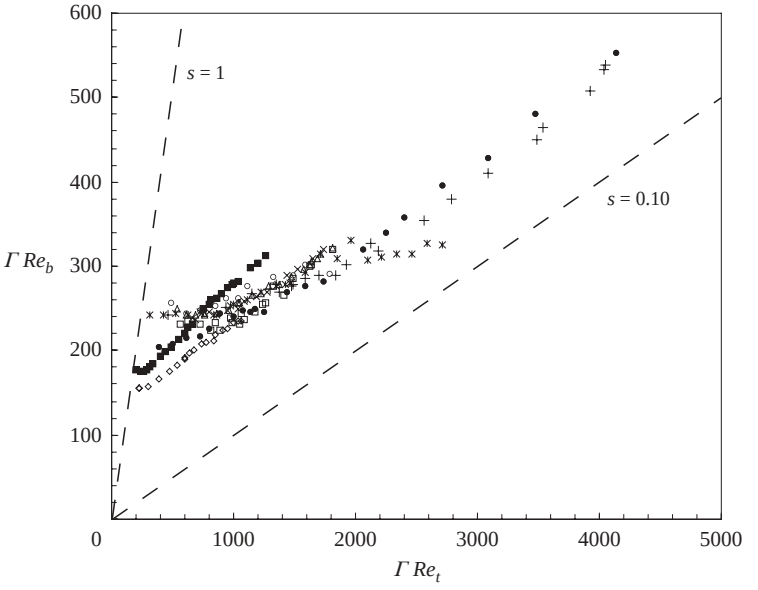

FIGURE 8. Stability curves. Same data as in figure 7, but plotted in the (ΓRe_t, ΓRe_b) plane of parameters. The axisymmetric base flow is stable in the lower region.

rotation ratio for the onset of the two-cell structure, which takes place at $s_0 \approx 0.10$ for high Reynolds numbers.

The approximate collapse of the onset curves in figure 7 indicates that the polygon pattern and the negative spirals arise from the same instability mechanism, a shear layer instability, although the nonlinear saturation leads to very a different morphology. Taking the shear $\Omega R/h$ as an estimate for the growth rate of the instability, and h^2/ν for the damping timescale, then the natural control parameter is $(\Omega R/h)h^2/\nu \sim \Gamma Re$. This is a rough estimate, since the instability takes place for radii that may be much lower than the cell radius R, but it is supported well by the approximate collapse of the data observed for $\Gamma \geqslant 4$.

As the sidewall rotates with one of the two disks, the flow configuration is not invariant by reflection with respect to the horizontal plane. The influence of the sidewall is expected to be negligible in the limit of large aspect ratio Γ, but may be significant for the range of Γ spanned in the present study. It may therefore be of interest to compare the stability curve of the actual flow configuration with that of the symmetric configuration. We call *configuration A* (resp. *B*) the situation where the sidewall rotates with the faster (resp. slower) disk. Figure 9(*a*) shows the stability curve in configurations A and B for an aspect ratio $\Gamma = 7.2$ in the plane of parameters (Re_{fast}, Re_{slow}), the Reynolds numbers based respectively on the faster and slower rotating disk.

The thresholds in configuration B appear to be around 10% lower than that of configuration A, with no significant trend as the Reynolds number is varied. In configuration A, the fluid rotation due to the faster disk is sustained by the co-rotating sidewall, and the resulting flow at the periphery of the cell is closer to a solid-body rotation. As a result, the stagnation circle where the centrifugal effects of each disk balance is smaller, and the internal shear layer is weakened, so that configuration A is more stable than B. The normalized threshold difference $(Re_{\mathrm{slow},A} - Re_{\mathrm{slow},B})/Re_{\mathrm{slow}}$, plotted as a function of the aspect ratio in figure 9(*b*), shows a decrease proportional

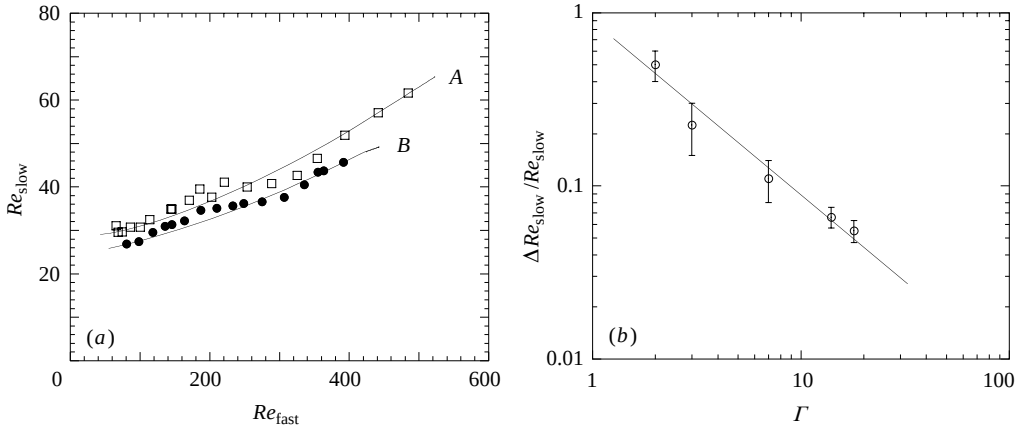

FIGURE 9. (*a*) Stability curves for an aspect ratio $\Gamma = 7.2$. □, Configuration *A*: the sidewall rotates with the faster disk; ●, Configuration *B*: the sidewall rotates with the slower disk. (*b*) Relative deviation of the threshold between configurations *A* and *B* as a function of Γ. The line shows $0.9\Gamma^{-1}$, and the error bars reflect the variability of the deviation along the curves from (*a*).

to Γ^{-1}, indicating that the boundary condition at $r = R$ has an influence of order of h/R on the instability threshold. This difference between configurations *A* and *B* remains small for high aspect ratio, and in the following we will restrict ourselves to the configuration *A*.

5.3. *Numerical and experimental description of the flow patterns*

In order to obtain further insight into the instability mechanism of the counter-rotating flow, PIV measurements and numerical simulations have been performed close to the onset.

Figure 10 shows the horizontal velocity field and the associated vertical vorticity field, measured by PIV at mid-height, $z = h/2$, for $\Gamma = 7$. As previously, only one quarter of the velocity vectors are shown, and the vorticity colour map has been rescaled by the angular velocity of the top disk. Figure 10(*a*) shows the axisymmetric base flow, while the three bifurcated fields in (*b*), (*c*) and (*d*) show azimuthal modulations of modes $m = 5$, 4 and 3, obtained for increasing (Re_t, Re_b) along the onset curve. The annular shear layer is found to evolve towards a sharp-cornered polygonal pattern, each side containing a local minimum and maximum of vorticity. The modulation of the vorticity level along the shear layer is similar to the classical Kelvin–Helmholtz 'cat's eyes' pattern for the linear case. The vorticity maxima are located slightly downstream of the corners of the polygon, which probably results from a nonlinear deformation of an initially symmetric chain of vorticity extrema. Flatter cavities (figures 11*a*, for $\Gamma = 9.3$, and 11*b*, for $\Gamma = 14$) show the same modulated shear layer, but the vertical confinement leads to a saturated pattern that becomes more complex than the one observed for low Γ. In addition to the polygonal shear layer, a set of m inner spiral arms appears in the centre of the flow, where local vorticity minima, of the same sign as the slower rotating disk, becomes concentrated.

Because of the above-mentioned limitations of the PIV measurements, the structure of the vorticity field for even flatter cavities can only be investigated from the numerical simulations. For $\Gamma = 21$, illustrated in figure 12, the annular shear layer appears to be much thinner, leading to a higher-order mode, here $m = 11$. The

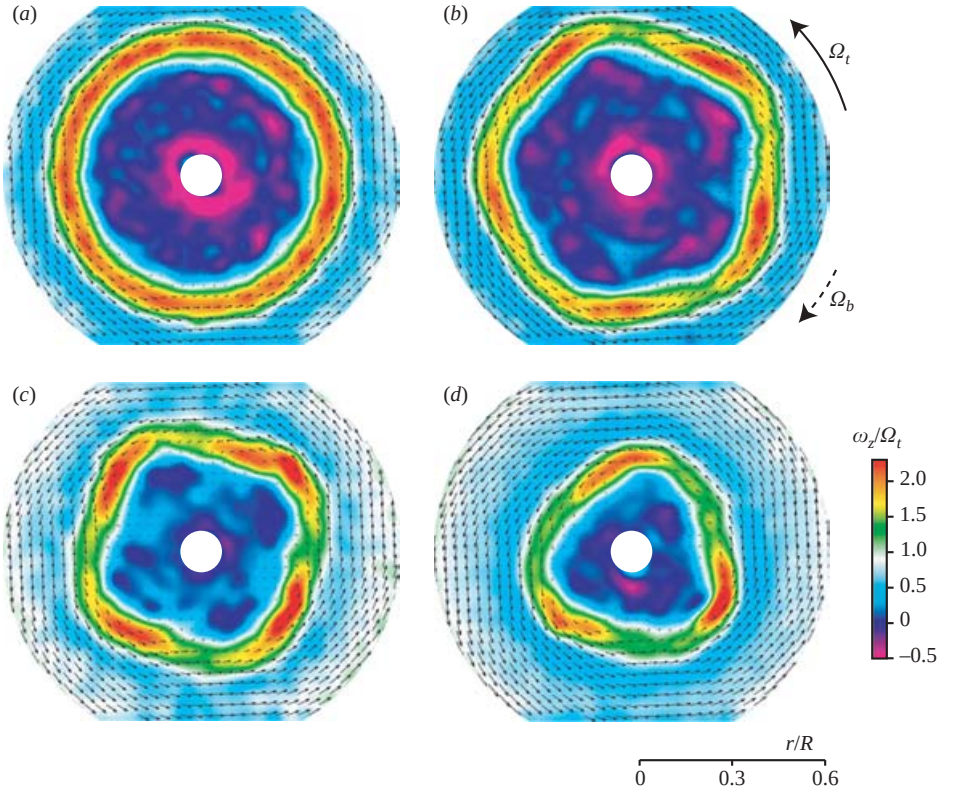

FIGURE 10. Experimental velocity and vorticity fields ω_z at mid-height $\Gamma = 7$; (*a*) is below the onset, and (*b–d*) are for increasing Reynolds numbers along the onset curve. (*a*) $(Re_t, Re_b) = (240, 40)$; (*b*) (240, 43); (*c*) (289, 45); (*d*) (341, 50).

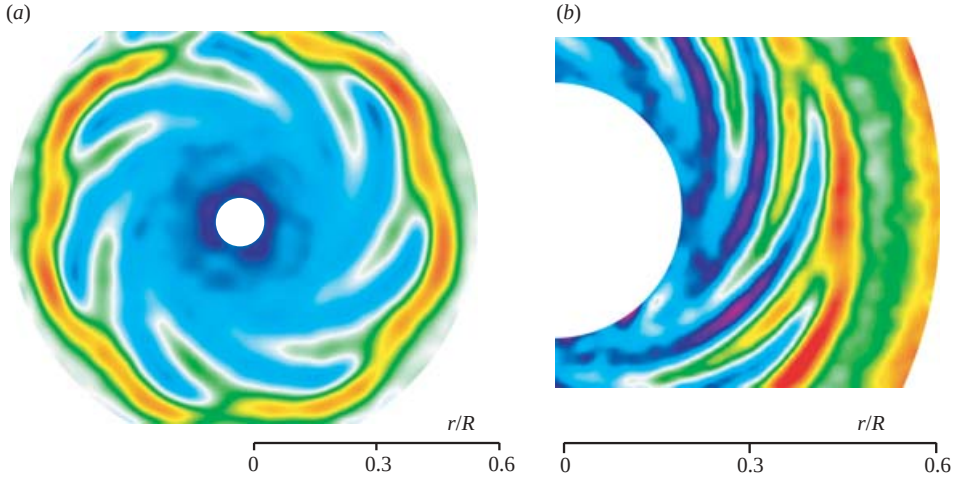

FIGURE 11. Experimental vorticity fields ω_z at mid-height. (*a*) $(\Gamma, Re_t, Re_b) = (9.3, 183, 28.5)$, mode $m = 7$. (*b*) (14, 80, 19), mode $m = 8$. The colour maps are the same as in figure 10.

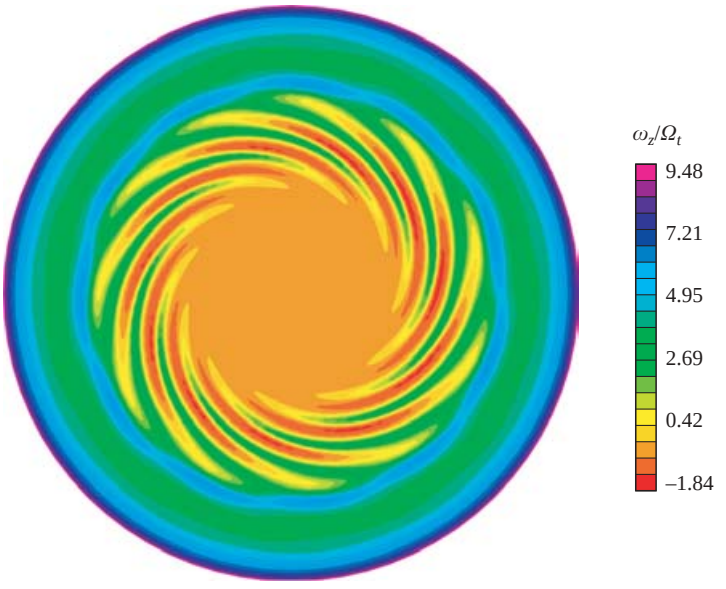

FIGURE 12. Numerical axial vorticity field ω_z at mid-height $z = h/2$ for $\Gamma = 21$, $Re_t = 67$, $Re_b = 14.3$, showing a mode $m = 11$. Only the central region $r \leqslant 0.95R$ is shown.

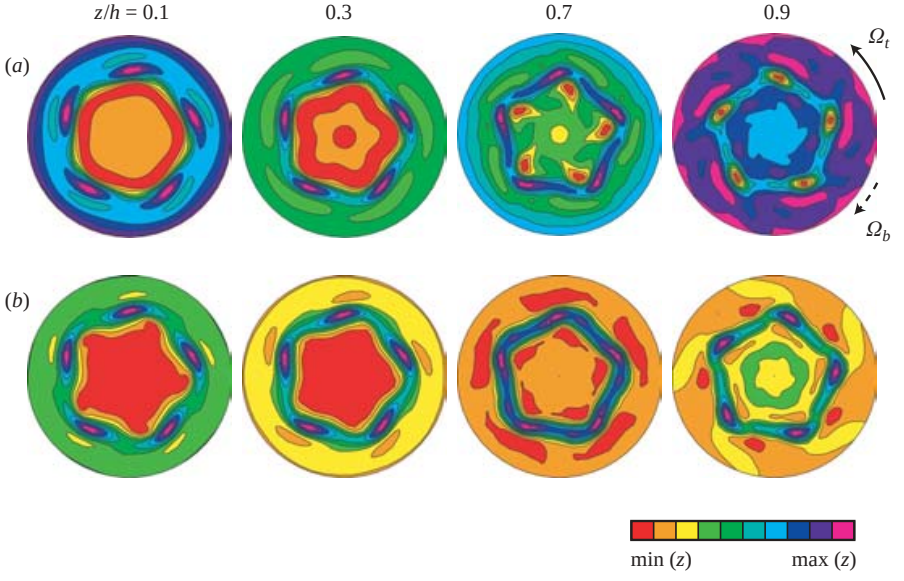

FIGURE 13. Numerical axial vorticity ω_z (a) and axial velocity v_z (b) at different heights $z/h = 0.1$ (close to the slower disk), 0.3, 0.7 and 0.9 (close to the faster disk), for $\Gamma = 7$, $Re_t = 250$, $Re_b = 57$, showing a mode $m = 5$. The colour maps for both ω_z and v_z are normalized by their minimum and maximum on each field. Only the central region $r/R \leqslant 0.6$ is shown.

similarity with the visualization in figure 6(e) is remarkable. Only the m inner spiral arms can be seen, suggesting that the $2m$ outer spiral arms are outside the mid-height plane.

The three-dimensional structure of the pattern can be inferred from the numerical vertical vorticity and velocity fields shown in figure 13 for $\Gamma = 7$, for heights z ranging

from $0.1h$ (close to the slower disk) up to $0.9h$ (close to the faster disk). From these figures, the vertical structure of the polygonal shear layer and the influence of the boundary layers of each disk can be seen.

It is remarkable that the locations of the vorticity extrema approximately coincide for each field, suggesting that the flow structure is roughly invariant along the vertical direction, except close to the disks where the boundary layers occur. Along these columnar vortices strong upward flow is present, which advects negative vorticity from the bottom to the top disk. Close to the faster disk (4th slice), the outer spiral arms appear surrounding the polygonal shear layer. Slight vorticity modulations show $2m$ extrema along the azimuthal direction, similar to the $2m$ outer spiral arms seen in figure 6(c). These spiral arms result from the interaction of the shear layer primary instability pattern in the bulk of the flow with the centrifugal Ekman boundary layer over the faster disk. The Ekman layer advects the perturbation outwards with an anticlockwise rotation, resulting in the observed negative spirals. Since they are mainly localized near the top disk, these negative spirals can clearly be seen in the seeding flakes visualizations in figure 6, although they are associated with very weak vorticity modulation.

5.4. *Growth rates and nonlinear saturation of the instability*

We now investigate the growth rates and the nonlinear saturation of the bifurcated flow slightly above the onset. The energy of the instability pattern may be defined as the difference between the total energy of the flow and the energy of the unstable axisymmetric base flow. Since the unstable base flow obviously cannot be deduced from experimental measurements of the bifurcated flow, we approximate it by the azimuthal average of the total energy. Note that we are only dealing with the contribution of the horizontal components of the velocity at a given height, since the vertical component is not accessible from the present two-dimensional PIV measurements. Within these approximations, the energy per unit mass of the bifurcated flow at a given height can be written

$$\Delta E = \frac{1}{2}\frac{1}{\pi R^2}\int_0^{2\pi}\int_0^{R}\{[v_r(r,\theta)-\bar{v}_r(r)]^2+[v_\theta(r,\theta)-\bar{v}_\theta(r)]^2\}r\,\mathrm{d}r\,\mathrm{d}\theta, \qquad (5.1)$$

where the overbars denote the azimuthal average of the horizontal components of the instantaneous velocity field. Since the bifurcated state is very sensitive to the distance to the threshold, the PIV measurements have been performed at small aspect ratio, $\Gamma = 3$, where a wider range of Reynolds numbers can be explored before secondary instabilities occur. For this aspect ratio the pattern is confined to small radii, and the radial integration in equation (5.1) has been restricted to the range $0 \leqslant r \leqslant 0.64R$.

Figure 14(a) shows the energy ΔE as a function of time for a fixed value $Re_t = 280$, after a sudden increase of Re_b at $t \approx 0$, from a value slightly below the threshold, 70, up to values between 75 and 79. At $t = 0$, the flow is axisymmetric, and the non-zero value of ΔE simply corresponds to the noise level of the PIV measurements and the azimuthal average procedure. For $Re_b \in [75, 78]$, after a transient growth, the energy saturates towards a constant value, ΔE_s, which is plotted in figure 14(b) as a function of Re_b. The corresponding flow patterns are shown in figure 15. Above the instability threshold, $Re_{b,c} \approx 74$ here, the energy linearly increases proportionally to $Re_b - Re_{b,c}$, as expected for a supercritical bifurcation. Similar results were reported by Gauthier *et al.* (2002) in the case $\Gamma = 20.9$, and we believe that the bifurcation remains supercritical for the whole range of aspect ratio spanned in this paper. For

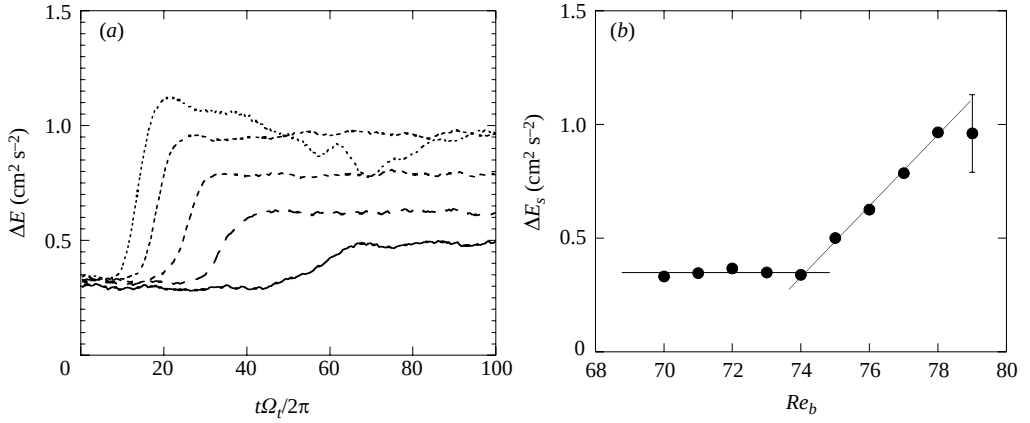

FIGURE 14. (a) Energy of the non-axisymmetric part of the flow, equation (5.1), as function of time, after a sudden increase of Re_b at $t = 0$ s from 70 to 75, 76, 77, 78 and 79 (from solid line to short-dashed line), computed from the velocity fields of figure 15 ($\Gamma = 3$ and $Re_t = 280$). (b) Energy of saturation of the bifurcated state as a function of Re_b.

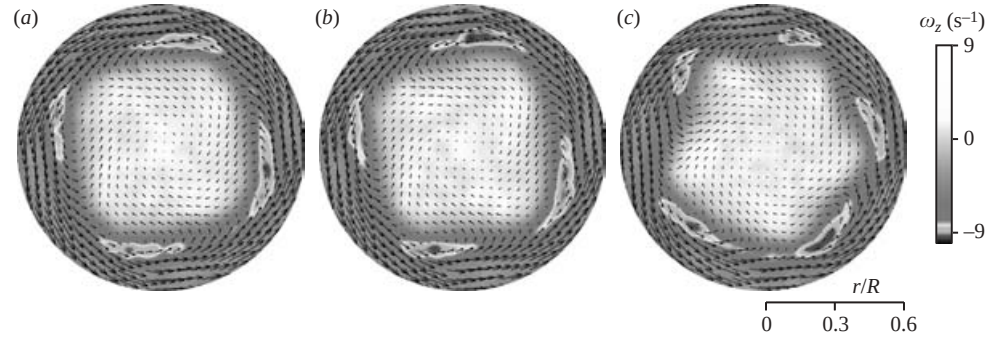

FIGURE 15. Experimental velocity and vorticity fields for $\Gamma = 3$ and $Re_t = 280$. (a) $Re_b = 75$; (b) $Re_b = 77$; (c) $Re_b = 79$. The grey scale has been chosen in order to emphasize the local vorticity extrema of the shear layer.

$Re_b = 79$, the pattern is a non-steady combination of modes $m = 4$ and 5 (figure 15c), and ΔE does not show saturation, as depicted by the error bar in figure 14(b).

Linear computations have been performed for the same flow parameters, $\Gamma = 3$ and $Re_t = 280$, in order to provide further insight into the observed modes. Figure 16 shows the growth rate σ of each mode as a function of Re_b. The most unstable mode is $m = 3$ at $Re_b = 72.3$, but it is closely followed by the mode $m = 4$, which becomes more unstable for $Re_b > 73.9$. This mode $m = 3$ was not observed experimentally, probably due to our limited resolution on the Reynolds numbers, of order of 3%. If Re_b is further increased, the dominant mode becomes $m = 5$, for $Re_b = 78.9$, in good agreement with the experiment (figure 15). Note that the growth rates cannot be inferred from the experimental measurements of figure 14(a), because only the very late time before saturation can be observed experimentally, and the earlier exponential growth falls largely below the experimental noise level.

The numerically observed modes for $\Gamma = 3$ and 7 are summarized in the marginal stability curves in figure 17. The experimentally observed modes at $\Gamma = 3$ are also shown for comparison. In both cases the critical mode is $m = 3$. These curves show the

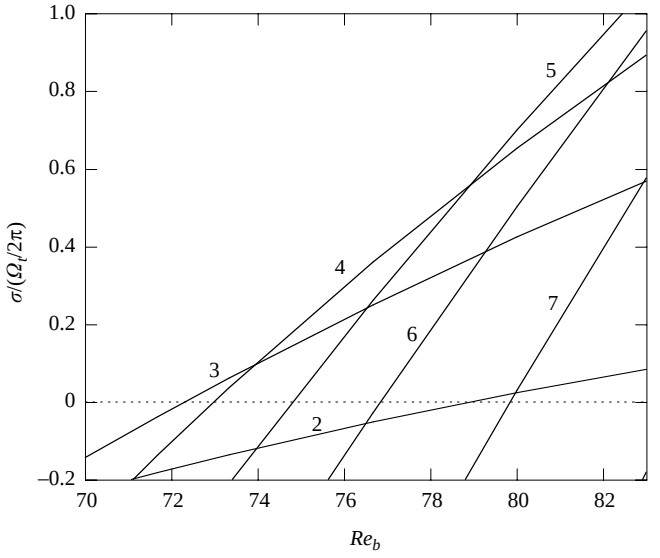

FIGURE 16. Non-dimensional growth rate of the different modes as a function of Re_b, for $\Gamma = 3$, $Re_t = 280$.

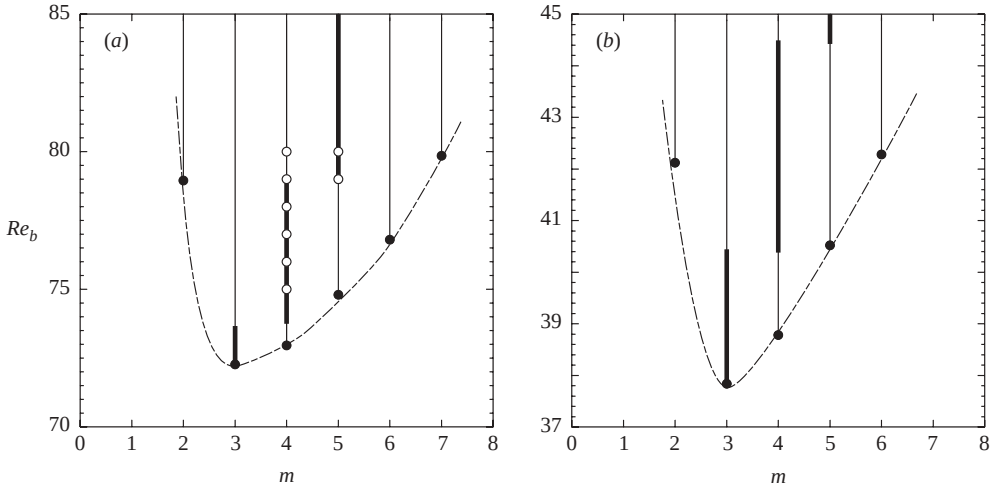

FIGURE 17. Marginal stability curves obtained from the linear computations for $Re_t = 280$. ●, critical Reynolds number Re_b for a given mode m; thick line, most unstable mode. The dashed curve joining the points is guide for the eye. (*a*) $\Gamma = 3$, $Re_{b,c} = 72.3$; ○, experimentally observed modes. (*b*) $\Gamma = 7$, $Re_{b,c} = 37.8$.

important sensitivity of the most unstable mode slightly beyond the instability threshold. This sensitivity remains of the order of the experimental uncertainty, around 3%, making difficult any accurate determination of the onset mode. The restricted range of experimentally observed modes compared to the linearly unstable modes may be the result of a nonlinear wavenumber selection, such as the Eckhaus instability (Ahlers *et al.* 1986).

Since in the experiment the Reynolds number cannot be kept close to the transition, one may expect nonlinearities to significantly affect the selected modes. In order to

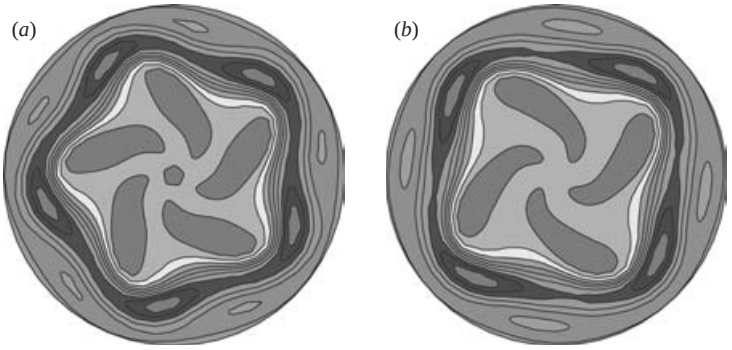

FIGURE 18. Iso-vorticity levels at mid-height obtained for the same parameters, $\Gamma = 3$, $Re_t = 280$, $Re_b = 80$, starting from different initial conditions: (*a*) from sudden increase of Re_b from 70, showing a mode $m = 5$; (*b*) from progressive increase of Re_b from 70, showing a mode $m = 4$. Only the central circle $r \leqslant 0.65R$ is shown.

check this point, nonlinear computations have been performed at $\Gamma = 3$, $Re_t = 280$ and $Re_b = 80$, i.e. 11% beyond the transition. For these values, linear computations show that the modes $m = 2$ to 7 are unstable, the most unstable being the mode $m = 5$ (see figure 16).

Figure 18 shows the long-time evolution of two computations performed for the same flow parameters, which differ only by the initial condition. The axisymmetric stable flow for $Re_b = 70$ is taken as the initial condition for the first computation (figure 18*a*), in a similar way as for the experiments, where Re_b was suddenly increased from 70 to a value above the threshold. For the second computation (figure 18*b*), the bottom Reynolds number has been gradually increased from 70 up to 80 in four steps, waiting for the saturation of the flow at each step (typically 300 rotation periods of the faster disk). While the first computation (*a*) shows a mode $m = 5$, the second one (*b*) shows a mode $m = 4$. For similar values of Re_b (see figure 15*c*), the experiment shows a mixed state, dominated by modes 4 and 5. The progressive increase of Re_b in the second case probably constrained the flow to follow the metastable branch $m = 4$, although other branches may be more unstable. These observations clearly illustrate the sensitivity of the observed pattern to the initial condition. They are in good agreement with a number of experimental observations, where strong hysteresis is observed for the modes, although no hysteresis is present in the value of the threshold. This situation is generic for systems where the geometrical confinement leads to azimuthal wavenumber quantization (see, e.g., Rabaud & Couder 1983).

6. Characterization of the shear layer instability

6.1. *Local control parameter for the shear layer instability*

The experimental and numerical vorticity fields in figures 10–13 indicate that the basic mechanism responsible for the observed flow pattern is a shear layer instability. In order to confirm this observation, and to test any possible influence of the curvature, the local Reynolds number Re_l based on the thickness w of the shear layer and the velocity jump ΔU across it can be computed:

$$Re_l = \Delta U w / \nu. \tag{6.1}$$

It is expected that, just below the onset of the instability, this local Reynolds number reaches a unique critical value.

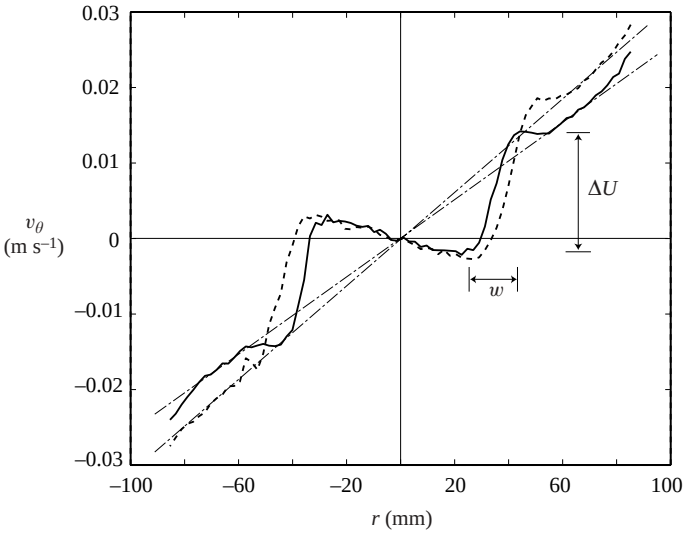

FIGURE 19. Azimuthal velocity profiles $v_\theta(r)$ computed from PIV fields at mid-height $z = h/2$, measured just below the onset of instability, for $\Gamma = 7$. – –, $Re_t = 239$; —, $Re_t = 277$. The corresponding solid-body rotation profiles $v_\theta(r) = 0.3\Omega_t r$ are also shown for both Re_t (– - –). Only the central circle $r \leqslant 0.6R$ is measured. The definitions of the shear layer thickness w and velocity jump ΔU are sketched for the curve —.

A series of PIV measurements for $\Gamma = 7$ along the onset curve has been performed, and the shear layer thickness and velocity difference have been extracted from the velocity fields. Figure 19 shows two azimuthal velocity profiles, averaged over $[0, \pi]$ (negative r corresponds to the other half $[\pi, 2\pi]$). The two profiles correspond to two different top Reynolds numbers but, in each case, the bottom Reynolds number has been set just below its corresponding critical value. Both profiles consist of two sections of quasi-solid-body rotation separated by a rather sharp velocity front. The inner region rotates in the direction of the slower disk, with an angular velocity of about $-0.5\Omega_b$, and the outer region rotates with the faster disk, at $\sim 0.3\Omega_t$. While the former value probably strongly depends on the height z, it is interesting to note that the latter value is close to the angular velocity found in the inviscid core of the Batchelor (1951) flow, $v_\theta(r) \approx 0.313\Omega_t r$ (see Zandbergen & Dijkstra 1987).

From this figure the velocity jump ΔU is computed as the difference between the surrounding extrema across the front, and the thickness w as the distance between these extrema. Only the horizontal projection of the thickness is actually measured. However, since the shear layer was shown to be almost vertical (see the numerical vorticity fields in figure 13), at least for moderate Γ, the apparent thickness gives a reasonable estimate for the actual one. This thickness is found to be of order the gap between the disks, $w \approx (0.6 \pm 0.1)h$, and shows no significant variation with the Reynolds number. The scaling $w \propto h$, although not tested experimentally for other aspect ratios, is in qualitative agreement with experimental and numerical fields (see figures 11 and 12), from which the shear layer thickness appears to decrease as Γ is increased.

The local Reynolds number computed from these measurements is shown in figure 20(a) as a function of Re_t. Although Re_t is varied from 140 to 370, Re_l remains approximately constant, giving evidence that this Reynolds number is the relevent local control parameter for the instability. The scatter is significant, and is mainly due

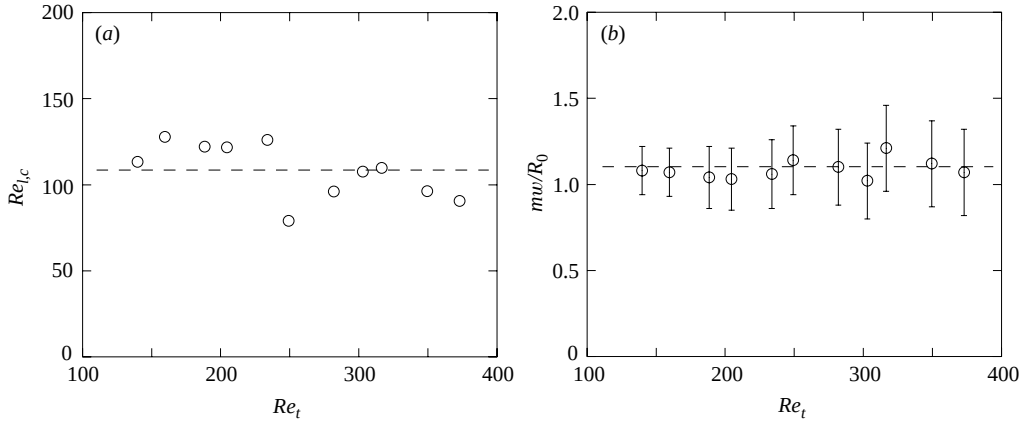

FIGURE 20. (*a*) Critical local Reynolds number $Re_{l,c}$ based on the shear layer thickness as a function of Re_t for $\Gamma = 7$. For each measurement, the bottom Reynolds number Re_b is fixed to its transition value. (*b*) Corresponding normalized wavenumber $m\,w/R_0$.

to the precision in the measurement of w, but the critical local Reynolds number can be estimated as

$$Re_{l,c} \approx 110 \pm 20. \tag{6.2}$$

This value is in qualitative agreement with the threshold $Re \approx 85 \pm 10$ measured by Rabaud & Couder (1983) from the circular shear layer experiment. Our slightly higher value may be due to the overestimation of the apparent shear layer thickness, or to some stabilizing effect due to the particular geometry of the annular shear layer. It is worth pointing out that, for the range of Reynolds number Re_t spanned here, the relative curvature of the shear layer, w/R_0 (where R_0 is the shear layer radius), increases from 0.16 to 0.52. However, this important variation does not significantly affect the threshold Re_l, suggesting that the curvature has only weak effect on the stability of this shear layer.

The approximate collapse of the onset curves in the plane of parameters (ΓRe_t, ΓRe_b), observed in figure 8, follows from this constant Re_l at the onset. Taking $R_0\Omega_t$ as an estimate for the velocity jump ΔU, and using $w \sim h$ for the shear layer thickness, then the condition $Re_l = \Delta U w/\nu \approx$ const simply yields $R_0 h \Omega_t/\nu = \Gamma Re_t R_0/R \approx$ const, confirming the experimental finding that the Reynolds numbers ΓRe_i are the most relevant global control parameters to describe the onset curves. However, the link between the global and local control parameters, ΓRe_t and Re_l, remains non-trivial because of the additional ratio R_0/R, and may account for the systematic deviations observed in figure 8.

One consequence of this shear layer instability mechanism is that the critical wavelength should scale as the thickness w of the shear layer (Drazin & Reid 1979). As a result, the number of vortices along the shear layer is expected to scale as $2\pi R_0/w$. This is indeed the case, as shown in figure 20(*b*), where the normalized wavenumber mw/R_0 is plotted as a function of Re_t. The observed constant value,

$$\frac{m\,w}{R_0} \approx 1.10 \pm 0.15, \tag{6.3}$$

confirms this picture, leading to a wavelength $\lambda = 2\pi R_0/m \approx (5.7 \pm 0.8)w$. Here again this finding compares well with the circular shear layer experiment of Rabaud & Couder (1983), for which the shear layer radius is constrained by the geometry of the

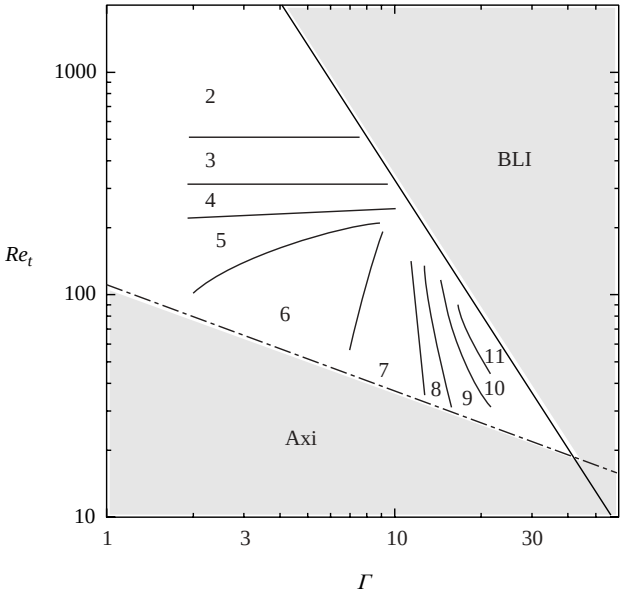

FIGURE 21. Experimental regime diagram of the onset modes in the plane (Γ, Re_t), where $\Gamma = R/h$ is the aspect ratio and Re_t the top Reynolds number (the bottom Reynolds number, Re_b, is fixed at its transition value). The numbers indicate the onset modes, and the transition lines separate regions of constant onset mode. Modes between $m = 2$ and 11 are observed, for Γ between 2 and 21. In the upper region, denoted BLI ($Re_t > 31 \times 10^3 \Gamma^{-2}$), boundary layer instabilities occur in addition to the shear layer instability. In the lower domain, denoted Axi ($Re_t < 105\Gamma^{-1/2}$), the axisymmetric base flow remains stable.

apparatus. In the present rotating disks experiment, this radius R_0 is not fixed, but is determined by the competition of the centrifugal effects on each disk.

From the $m \propto R_0$ law observed here for $\Gamma = 7$, one may deduce that the onset mode is a decreasing function of Re_t, since the increasing centrifugal effect of the faster disk tends to decrease the radius of the shear layer R_0. This is indeed the case (see, e.g., figure 10), at least for moderate aspect ratios Γ; for higher aspect ratios the interaction with the boundary layers significantly affects this behaviour, as shown in the next section.

6.2. *Onset modes*

The observed modes are found to depend not only on the Reynolds numbers and the aspect ratio, but also on the time history of the control parameters (Re_b, Re_t), as shown in § 5.4. As a consequence, the only quantity that may be summarized is the critical mode that first becomes unstable just at the onset when slowly approaching the onset curve from below.

Figure 21 shows the experimental regime diagram for the onset mode in the plane of parameters (Γ, Re_t). For each value of the top Reynolds number, Re_t, the bottom Reynolds number, Re_b, has been fixed at its corresponding critical value (see figure 7), so that the set of three parameters (Γ, Re_t, Re_b) reduces to two. In this diagram, the lines delimit regions where a unique onset mode is experimentally observed. As noted in § 5.4, the sensitivity of the observed mode slightly beyond the onset curve is important (see figure 17), so that the observed mode m may occasionally overestimate the actual onset mode, shifting the transition lines between modes upwards.

This diagram is restricted to a triangle in the plane (Γ, Re_t). In the domain denoted Axi, below a line given by

$$Re_t \approx (105 \pm 9)\Gamma^{-1/2}, \tag{6.4}$$

the flow is found to remain axisymmetric. In this domain the shear layer is probably stabilized by the thick boundary layers that fill an important part of the vertical gap, but no simple argument is found to explain the observed $\Gamma^{-1/2}$ behaviour.

The domain above the upper line, denoted BLI for 'boundary layer instability', corresponds to the destabilization of the inward boundary layer on the slower rotating disk, giving rise to the propagating circles and positive spirals that have been described in detail by Gauthier *et al.* (2002). Since the boundary layer stability is controlled by a local Reynolds number, $Re_r = \Omega r^2/\nu$, an approximate condition for stability is that $Re_r < Re_c$ for all $r < R$, leading to a line $\Omega_t R^2/\nu = Re_c$, or equivalently

$$Re_t = \Omega_t h^2/\nu = Re_c \Gamma^{-2}. \tag{6.5}$$

This is indeed the case, and we determine experimentally $Re_c \approx (31 \pm 2) \times 10^3$. Note that although measurements of the critical mode were sometimes possible slightly beyond this upper limit, we choose to restrict ourselves to the situation where the boundary layers remain stable.

For high Reynolds number, $Re_t > 200$ (i.e. only for $\Gamma < 12$), the transition lines between modes are nearly horizontal, i.e. the onset modes m are essentially controlled by the top Reynolds number, Re_t, and take values from 5 down to 2 as Re_t is increased. The corresponding flow pattern essentially consists of the sharp-cornered polygon, as seen in figure 6(*a–c*). The onset mode $m = 4$ reported by Lopez *et al.* (2002) for $(\Gamma, Re_t) = (2, 250)$ agrees with the $m = 4$ domain in figure 21, which extends between $Re_t = 230 \pm 10$ and 320 ± 20. In this regime, the boundary layers over each disk are well separated, $\delta = (\nu/\Omega_t)^{1/2} < h/12$, so that the dynamics of the annular shear layer can be seen as essentially two-dimensional. The onset mode then only depends on the shear layer radius R_0 and thickness $\delta \sim h$, in agreement with the law $m \propto R_0$ observed in the previous section for $\Gamma = 7$ (equation (6.3)). As a consequence, while the Reynolds number based on the azimuthal velocity, $\Gamma Re_t = Rh\Omega_t/\nu$, is the most relevant control parameter for the instability threshold (see figure 8), the Reynolds number $Re_t = h^2\Omega_t/\nu$ is the one that controls the onset mode in the $Re_t > 200$ domain.

For lower Reynolds numbers, $Re_t < 200$, this behaviour does not hold any more and the regime diagram becomes more complex. In this regime, the flow is fully three-dimensional, with thick boundary layers, $\delta > h/12$, that may strongly interact with the annular shear layer. The corresponding flow pattern now evolves towards the spiral arms of figure 6(*d–f*). As Γ is increased, the transition lines between modes become nearly vertical, and their slope becomes negative for $\Gamma > 12$. As a consequence, the critical mode is an increasing function of Re_t, in contrast to the low aspect ratio case. This new behaviour is in agreement with the results of Gauthier *et al.* (2002) at $\Gamma = 20.9$, where modes 9, 10 and 11 were reported for increasing Reynolds numbers.

We finally note that extrapolating the boundaries of the two domains Axi and BLI towards higher aspect ratio suggests that the shear layer instability described here should only be observed for $\Gamma < 40$. For higher aspect ratio, the boundary layers would become unstable as soon as they become separated, probably inhibiting or strongly affecting the shear layer instability. Other instability mechanisms may also appear for such high aspect ratios, such as the turbulent spots in the torsional Couette flow described by Cros & Le Gal (2002) in the rotor–stator configuration.

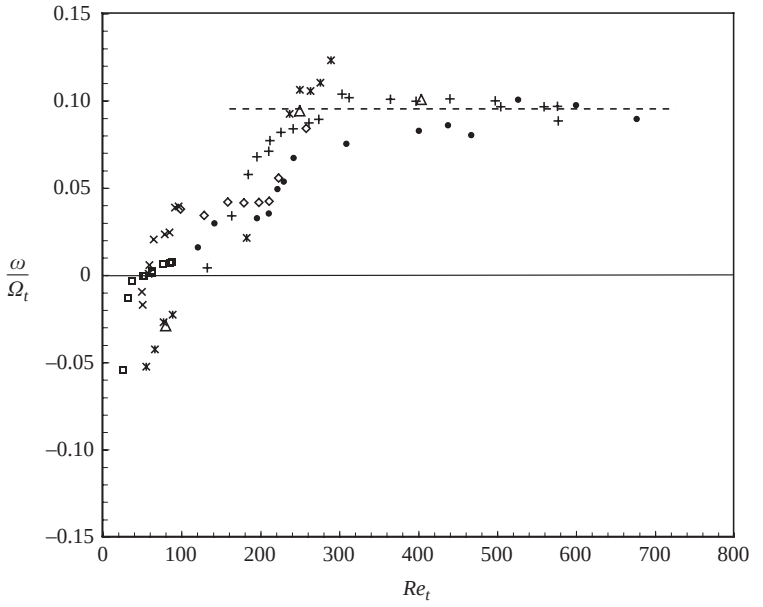

FIGURE 22. Normalized phase velocity ω/Ω_t at the onset as a function of Re_t for various aspect ratios Γ. Experiment: ◇, $\Gamma = 3$; ●, 5.2; +, 7; ⋆, 9.3; ×, 17; □, 20.9. Numerics: △, $\Gamma = 7$. The dashed line is $\omega/\Omega_t = 0.095$.

6.3. *Phase velocities*

Because of the asymmetry of the flow, the instability patterns are not steady, but rather appear as rotating waves, characterized by a well-defined drift velocity ω. Figure 22 shows the experimentally measured angular phase velocity at the onset, ω, normalized by the top angular velocity, Ω_t, as a function of Re_t for various aspect ratios. Values obtained from numerical simulations, for $\Gamma = 7$, are also plotted and are found to compare well with the experimental results. Although the scatter is significant, the different curves appear to collapse reasonably well. The phase velocity is found to increase, starting from slightly negative values for low Re_t, crossing zero for $Re_t \sim 50$–100, and finally saturating towards a constant positive value for $Re_t > 250$:

$$\frac{\omega}{\Omega_t} \approx 0.095 \pm 0.01. \tag{6.6}$$

For high Reynolds numbers, the shear layer can be seen as essentially two-dimensional, with no significant influence of the boundary layers. The constant phase velocity ω/Ω_t observed in this case is similar to the classical linear Kelvin–Helmholtz case, for which the phase velocity is given by the average of the two stream velocities (Drazin & Reid 1979). Extending this result to the annular case yields $\omega = (\Omega_1 + \Omega_2)/2$, where Ω_1 and Ω_2 are respectively the inner and outer angular velocities on each side of the shear layer. These angular velocities are non-trivial functions of the bottom and top disk velocities, Ω_b and Ω_t. However, a rough estimate for ω may be obtained by neglecting Ω_1, and taking $\Omega_2 \approx 0.3\Omega_t$ as for the classical Batchelor flow (see figure 19). These approximations yield $\omega/\Omega_t \approx 0.3/2 \approx 0.15$, which is in reasonable agreement with the observed limit, $\omega/\Omega_t \approx 0.095 \pm 0.01$. The much lower values for ω found in the lower Reynolds number regime, $Re_t < 250$, probably result from the

interaction with the thicker boundary layers, which tend to slow down the pattern rotation.

7. Conclusion

This paper describes a joint laboratory and numerical study of the instability patterns in the flow between counter-rotating disks, spanning a range of aspect ratio $\Gamma = R/h$ between 2 and 21. This study is restricted to the situation where the boundary layers remain stable, focusing on the shear layer instability that occurs only in the counter-rotating regime. For sufficiently large counter-rotation, the shear layer that separates two regions of opposite angular velocities is prone to an azimuthal symmetry breaking. The associated pattern is a combination of a sharp-cornered polygonal shear layer with m vorticity extrema, surrounded by a set of m inner and $2m$ outer spiral arms. At small aspect ratio and large velocity, only the m-sided polygon is observed, where the mode m decreases as the top Reynolds number is increased. On the other hand, for higher Γ, only the spiral arms remain, their number now increasing as the top Reynolds number is increased. These observations are in remarkable agreement with the three-dimensional numerical simulations performed for the same values of the parameters (Γ, Re_t, Re_b).

Focusing on the low aspect ratio case, $\Gamma < 10$, where PIV measurements are possible, we further characterized the instability in terms of local Reynolds number Re_l based on the shear layer thickness w. The constant value of this Reynolds number at the onset of the instability, $Re_{l,c} \approx 110 \pm 20$, confirms that the transition originates from a shear layer instability. Consequently, the critical mode m scales as R_0/w, where R_0 is the radius of the annular shear, which results from the competition between the centrifugal effects of each disk. In other words, the instability patterns can be simply seen as a set of vortices of size $\sim w$ regularly filling the shear layer perimeter. As a result, the onset mode is a decreasing function of the Reynolds number, since the shear layer radius decreases as the faster disk becomes more dominant.

All these findings indicate that this instability of the flow between counter-rotating disks can simply be described in terms of a classical Kelvin–Helmholtz instability, where curvature has only a weak effect, and that the surrounding spiral arms result from the interaction of this unstable shear layer with the Ekman boundary layers over the faster disk. These observations for various aspect ratios reveal the continuity between the patterns observed by Lopez *et al.* (2002) for $\Gamma \leqslant 2$ and the 'negative spirals' of Gauthier *et al.* (2002) for $\Gamma = 21$.

We gratefully acknowledge G. Gauthier, P. Gondret, G. M. Homsy, C. Nore, L. S. Tuckerman and J. E. Wesfreid for fruitful discussions. We are indebted to G. Chauvin, R. Pidoux and C. Saurine for experimental help. The computations were carried out on the NEC-SX5 computer of the Institut du Développement et des Ressources en Informatique Scientifique (IDRIS) of the Centre National pour la Recherche Scientifique (CNRS) (project no. 0327).

REFERENCES

Ahlers, G., Cannell, D. S., Dominguez-Lerma, M. A. & Heinrichs, R. 1986 Wavenumber selection and Eckhaus instability in Couette-Taylor flow. *Physica* D **23**, 202–219.

Batchelor, G. K. 1951 Note on a class of solutions of the Navier–Stokes equations representing steady rotationally–symmetric flow. *Q. J. Mech. Appl. Maths* **4**, 29–41.

Barbosa, E. & Daube, O. 2001 A finite differences method in cylindrical coordinates for 3D incompressible flows. *ECCOMAS CFD Conference, Swansea, UK* (CD-ROM ISBN 0905 091 12 4).

Bergeron, K., Coutsias, E. A., Lynov, J. P. & Nielsen, A. H. 2000 Dynamical properties of forced shear layers in an annular geometry. *J. Fluid Mech.* **402**, 255–289.

Blackburn, H. M. & Lopez, J. M. 2002 Modulated rotating waves in an enclosed swirling flow. *J. Fluid Mech.* **465**, 33–58.

Chomaz, J. M., Rabaud, M., Basdevant, C. & Couder, Y. 1988 Experimental and numerical investigation of a forced circular shear layer. *J. Fluid Mech.* **187**, 115–140.

Cros, A. & Le Gal, P. 2002 Spatiotemporal intermittency in the torsional Couette flow between a rotating and a stationary disk. *Phys. Fluids* **14**, 3755–3765.

Daube, O. & Le Quéré, P. 2002 Numerical investigation of the first bifurcation for the flow in a rotor-stator cavity of radial aspect ratio 10. *Computers Fluids* **31**, 481–494.

Dijkstra, D. & van Heijst, G. J. F. 1983 The flow between finite rotating disks enclosed by a cylinder. *J. Fluid Mech.* **128**, 123–154.

Dolzhanskii, F. V., Krymov, V. A. & Manin, D. Yu. 1990 Stability and vortex structures of quasi-two-dimensional shear flows. *Sov. Phys. Usp* **33** (7), 495–520.

Drazin, P. G. & Reid, W. H. 1979 *Hydrodynamic Instability*. Cambridge University Press.

Escudier, M. P. 1984 Observations of the flow produced in a cylindrical container by a rotating end wall. *Exps. Fluids* **2**, 179–186.

Früh, W. G. & Read, P. L. 1999 Experiments on a barotropic rotating shear layer. Part 1. Instability and steady vortices. *J. Fluid Mech.* **383**, 143–173.

Gadoin, E., Le Quéré, P. & Daube, O. 2001 A general methodology to investigate flow instabilities in complex geometries: application to natural convection in enclosures. *Intl J. Numer. Meth. Fluids* **37**, 175–208.

Gauthier, G., Gondret, P. & Rabaud, M. 1998 Motions of anisotropic particles: application to visualization of three-dimensional flows. *Phys. Fluids* **10**, 2147–2154.

Gauthier, G., Gondret, P. & Rabaud, M. 1999 Axisymmetric propagating vortices in the flow between a stationary and a rotating disk enclosed by a cylinder *J. Fluid Mech.* **386**, 105–126.

Gauthier, G., Gondret, P., Moisy, F. & Rabaud, M. 2002 Instabilities in the flow between co- and counter-rotating disks. *J. Fluid Mech.* **473**, 1–21.

Gelfgat, A. Y., Bar-Yoseph, P. Z. & Solan, A. 2001 Three-dimensional instability flow in a rotating lid–cylinder enclosure. *J. Fluid Mech.* **438**, 363–377.

Goda, K. 1979 A multistep technique with implicit difference schemes for calculating two or three dimensional cavity flows. *J. Comput. Phys.* **30**, 76–95.

Hide, R. & Titman, C. W. 1967 Detached shear layers in a rotating fluid. *J. Fluid Mech.* **29**, 39–60.

Humphrey, J. A. C., Schuler, C. A. & Webster, D. R. 1995 Unsteady laminar-flow between a pair of disks corotating in a fixed cylindrical enclosure. *Phys. Fluids* **7**, 1225–1240.

Hyman, J. M. & Shashkov, M. 1997 Natural discretization for the divergence, gradient and curl on logically rectangular grids. *Comput. Math. Appl.* **33**, 81–104.

von Kármán, T. 1921 Laminar und turbulente reibung. *Z. Angew. Math.* **1**, 233–252.

van de Konijnenberg, J. A., Nielsen, A. H., Rasmussen, J. J. & Stenum, B. 1999 Shear flow instability in a rotating fluid. *J. Fluid Mech.* **387**, 177–204.

Liou, W. W. 1994 Linear instability of curved free shear layers. *Phys. Fluids* **6**, 541–549.

Lopez, J. M. 1998 Characteristics of endwall and sidewall boundary layers in a rotating cylinder with a differentially rotating endwall. *J. Fluid Mech.* **359**, 49–79.

Lopez, J. M., Hart, J. E., Marques, F., Kittelman, S. & Shen, J. 2002 Instability and mode interactions in a differentially-driven rotating cylinder. *J. Fluid Mech.* **462**, 383–409.

Mamum, C. K. & Tuckerman, L. S. 1995 Asymmetry and Hopf bifurcation in spherical Couette flow. *Phys. Fluids* **7**, 80–91.

Marques, F., Gelfgat, A. Yu. & Lopez, J. M. 2003 Tangent double Hopf bifurcation in a differentially rotating cylinder flow. *Phys. Rev.* E **68**, 016310, 1–13.

Moisy, F., Pasutto, T. & Rabaud, M. 2003 Instability patterns between counter-rotating disks. *Nonlinear Processes Geophys.* **10**, 281–288.

Niino, H. & Misawa, N. 1984 An experimental and theoretical study of barotropic instability. *J. Atmos. Sci.* **41**, 1992–2011.

Nore, C., Tartar, M., Daube, O. & Tuckerman, L. S. 2004 Survey of instability thresholds of flow between exactly counter-rotating disks. *J. Fluid Mech.* (in press).

Nore, C., Tuckerman, L. S., Daube, O. & Xin, S. 2003 The 1:2 mode interaction in exactly counter-rotating von Kármán swirling flow. *J. Fluid Mech.* **477**, 51–88.

Rabaud, M. & Couder, Y. 1983 Instability of an annular shear layer. *J. Fluid Mech.* **136**, 291–319.

Schouveiler, L., Le Gal, P. & Chauve, M.-P. 2001 Instabilities of the flow between a rotating and stationary disk. *J. Fluid Mech.* **443**, 329–350.

Serre, E. & Bontoux, P. 2002 Vortex breakdown in a three-dimensional swirling flow. *J. Fluid Mech.* **459**, 347–370.

Serre, E., Crespo del arco, E. & Bontoux, P. 2001 Annular and spiral patterns in flows between rotating and stationary discs. *J. Fluid Mech.* **434**, 65–100.

Stewartson, K. 1953 On the flow between two rotating coaxial disks. *Proc. Camb. Phil. Soc.* **49**, 333–341.

Tuckerman, L. S. 1989 Steady-state solving via Stokes preconditioning: Recurrence relations for elliptic operators. *11th International Conference on Numerical Methods in Fluid Dynamics* (ed. D. L. Dwoyer, M. Y. Hussaini & R. G. Voigt). Lecture Notes in Physics, vol. 323, pp. 573–577. Springer.

Yanase, S., Flores, C., Métais, O. & Riley, J. J. 1993 Rotating free-shear flows. I. Linear stability analysis *Phys. Fluids* A **5**, 2725–2737.

Zandbergen, P. J. & Dijkstra, D. 1987 Von Kármán swirling flows. *Annu. Rev. Fluid Mech.* **19**, 465–91.